

Deep Learning the Quantum Phase Transitions in Random Electron Systems: Applications to Three Dimensions

Tomi Ohtsuki^{1*} and Tomoki Ohtsuki^{2†}

¹*Physics Division, Sophia University, Chiyoda-ku, Tokyo 102-8554, Japan*

²*NTT DATA Mathematical Systems Inc, Shinjuku-ku, Tokyo 160-0016, Japan*

Three-dimensional random electron systems undergo quantum phase transitions and show rich phase diagrams. Examples of the phases are band gap insulator, Anderson insulator, strong and weak topological insulators, Weyl semimetal, and diffusive metal. As in the previous paper on two-dimensional quantum phase transitions [J. Phys. Soc. Jpn. **85**, 123706 (2016)], we use image recognition algorithm based on multi-layered convolutional neural network to identify which phase the eigenfunction belongs to. Anderson model for localization-delocalization transition, Wilson-Dirac model for topological insulators, and layered Chern insulator model for Weyl semimetal are studied. The situation where the standard transfer matrix approach is not applicable is also treated by this method.

1. Introduction

Random three-dimensional (3D) electron systems show rich insulator and metal phases: band gap insulator, Anderson insulator,¹⁾ strong as well as weak topological insulator,^{2,3)} Weyl semimetal,^{4,5)} and diffusive metal are examples of the phases. The appearance of these phases^{2,3,6,7)} is related to the basic symmetry such as time reversal, spin rotation, chiral, and particle-hole symmetries.^{8–12)}

The eigenfunction of each phase exhibits specific features. In the Anderson insulator, the eigenfunctions are exponentially localized. Strong topological insulators exhibit two-dimensional (2D) Dirac electron on all the surfaces, while weak topological insulators show 2D Dirac electron on specific surfaces determined by weak indices.¹³⁾ In Weyl semimetal, surface states that form Fermi arc appear on surfaces parallel to the direction of split Weyl nodes.^{14–16)}

In the presence of randomness, however, owing to the large amplitude fluctuations of

*ohtsuki@sophia.ac.jp

†ootsuki_t@msi.co.jp

eigenfunctions, determining the phases from eigenfunctions becomes difficult, especially when the system is close to phase boundaries. It is to be noted that topological numbers are usually defined in the randomness-free systems via the integration of the Berry curvature of Bloch function over the Brillouin zone. The definition is no longer valid once the randomness is introduced, which breaks the translational invariance. Hence new definition of topological numbers in random systems is necessary.^{17–19)}

In the previous paper,²⁰⁾ we regarded the modulus squared (probability density) of an eigenfunction as an image, and used the image recognition²¹⁾ based on deep learning^{22,23)} to judge which phase the eigenfunction belongs to. Changing the stream of random numbers (MT2023) and their seeds, we have trained the convolutional neural network (CNN) by preparing large number of eigenfunctions belonging to each phase of random 2D electron systems, and have identified the phase of independently obtained eigenfunctions. The localization-delocalization transition in the presence of strong spin-orbit coupling (symplectic class),²⁴⁾ as well as Chern insulator-Anderson insulator transition (unitary class),^{16,25)} has been verified.

In this paper, we further advance this approach to deal with 3D systems. 3D systems show even richer phases than 2D, such as strong and weak topological insulators (STI/WTI) and Weyl semimetals (WSM). We will first study the Anderson type 3D localization-delocalization transition. Then the phase diagrams of topological insulators are derived, followed by the demonstration of phase diagram for layered Chern insulator that exhibits Chern insulators (CI), WSM, and diffusive metal (DM) phases. We will demonstrate that the phase diagram can be obtained even in cases where the transfer matrix approach^{26,27)} is not applicable.

2. Method

We consider four-weight-layer convolutional neural network, which outputs real numbers. Each number corresponds to the probability with which the input image belongs to certain phase. In the case of the Anderson transition, the output numbers are two, each corresponding to the probability of delocalized/localized phase. In the case of topological insulators, the output numbers are 4, corresponding to ordinary insulator (OI), WTI, STI, and DM. The output numbers are three for layered Chern insulator model, corresponding to CI, WSM, and DM.

We diagonalize 3D random electron systems on cubic lattice using sparse matrix diagonalization algorithm, Intel MKL/FEAST. We impose periodic boundary condition in y-

direction, and integrate the modulus squared of the eigenfunction $\psi(x, y, z)$ to obtain the input 2D image $F(x, z)$,

$$F(x, z) = \int dy |\psi(x, y, z)|^2. \quad (1)$$

The lengths in the x - and y -directions are 40, so the input image is 40×40 . The length in the y -direction is 40 for Anderson model and layered Chern insulator, 20 for topological insulator.

The four-weight-layer CNN used in this study is a variant of LeNet²⁸⁾ included in Caffe²⁹⁾ (with the input size changed to 40×40), which utilizes rectified linear unit (ReLU) as its activation function. The network weight parameters to be trained are sampled from Gaussian distribution of scale determined by the number of input and output dimensions,³⁰⁾ except for the first convolution layer connected to the input image: in the first convolution layer, we have manually chosen the weight initialization scale to be 100. This choice of weight initialization scale is due to the fact that we deal with eigenfunctions, the values of which are typically much smaller than those of gray-scale images.

We have used the RMSProp solver³¹⁾ with the parameters in the Caffe MNIST example (which is contained as `examples/mnist/lenet_solver_rmsprop.prototxt` in the Caffe source) as the stochastic gradient descent solver. During the training, we randomly partition the training data set into 90% and 10%, and use the latter as the validation set. The solver performs enough iterations so that the validation error becomes stationary. Further details can be found in the previous paper.²⁰⁾

3. Applications to 3D Quantum Phase Transitions

3.1 Anderson transition

We first use the 3D Anderson model of localization, and discuss the Anderson transition.¹⁾

The Hamiltonian is given by

$$H = \sum_x v_x c_x^\dagger c_x - \sum_{\langle x, x' \rangle} c_x^\dagger c_{x'}, \quad (2)$$

where c_x^\dagger (c_x) denotes the creation (annihilation) operator of an electron at site $x = (x, y, z)$, and v_x denotes the random potential at site x . $\langle \dots \rangle$ indicates the nearest neighbor hopping. We assume a box distribution with each v_x uniformly and independently distributed on the interval $[-W/2, W/2]$. At energy $E = 0$, i.e., at the band center, the wave functions are delocalized at $W < W_c$ and the system is a diffusive metal. For $W > W_c$, the wave functions are localized and the system is an Anderson insulator (AI). The value of W_c is estimated to be around 16.54 by the transfer matrix method combined with the finite size scaling analyses.³²⁾

As in the 2D symplectic case,²⁰⁾ we prepared 1000 eigenfunctions in diffusive metal regime and 1000 eigenfunctions in Anderson insulator regime. We then prepared independent 100 eigenfunctions with various strength of disorder W , and let the machine to judge whether they are delocalized (DM phase) or localized (AI phase). Results are shown in Fig. 1 (a), where the probabilities that the eigenfunction belongs to DM phase P_{DM} and to the AI phase $P_{\text{AI}} = 1 - P_{\text{DM}}$ are plotted as solid and dotted lines, respectively. Sharp transition from metal to insulator is observed near W_c .

As a test, we used the CNN trained for 2D DM–AI transition²⁰⁾ to judge the 3D eigenfunctions. Results are plotted in Fig. 1 (b), where the transition is qualitatively captured, although the transition occurs earlier than it should.

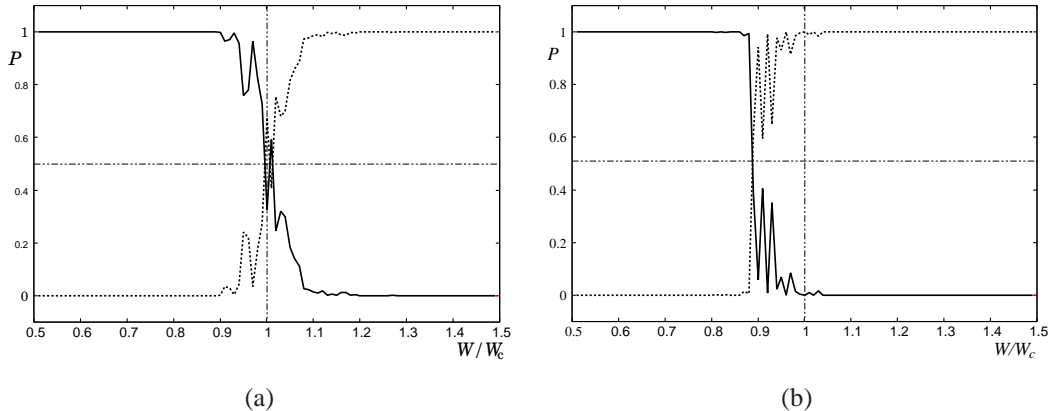


Fig. 1. Probabilities that the eigenfunction near the band center belongs to the delocalized phase (solid line) and to the localized phase (dotted line). Average over 5 samples are taken. (a) Results of learning the 3D Anderson transition and (b) those of learning the 2D Anderson transition. Dashed dotted lines indicate 50% probability (horizontal line) and the critical disorder (vertical line).

3.2 3D topological insulators

We next study the phases of 3D topological insulators. We consider the following Wilson-Dirac type tight-binding Hamiltonian,^{26,33)}

$$H = \sum_x \sum_{\mu=x,y,z} \left[\frac{it}{2} c_{x+\mathbf{e}_\mu}^\dagger \alpha_\mu c_x - \frac{m_{2,\mu}}{2} c_{x+\mathbf{e}_\mu}^\dagger \beta c_x + \text{H.c.} \right] + (m_0 + \sum_{\mu=x,y,z} m_{2,\mu}) \sum_x c_x^\dagger \beta c_x + \sum_x v_x c_x^\dagger 1_4 c_x, \quad (3)$$

where c_x^\dagger and c_x are four-component creation and annihilation operators on a site x , and \mathbf{e}_μ is a unit vector along μ -direction. α_μ and β are gamma matrices defined by

$$\alpha_\mu = \tau_x \otimes \sigma_\mu = \begin{pmatrix} 0 & \sigma_\mu \\ \sigma_\mu & 0 \end{pmatrix}, \quad \beta = \tau_z \otimes 1_2 = \begin{pmatrix} 1_2 & 0 \\ 0 & -1_2 \end{pmatrix}, \quad (4)$$

where σ_μ and τ_μ are Pauli matrices that act on spin and orbital degrees of freedom, respectively. m_0 is the mass parameter, and $m_{2,\mu}$ and t are hopping parameters. Random potential v_x is uniformly and independently distributed between $[-W/2, W/2]$. We set $m_{2,x} = m_{2,y} = 1$ as energy unit. The Hamiltonian belongs to the symplectic class for $W > 0$. We impose fixed boundary conditions in x - and z -directions.

We first set $t = 2$ and $m_{2,z} = 0.5$. In this case, ordinary insulator (OI) phase appears in $m_0 > 0$, strong topological insulator (STI) phase in $0 > m_0 > -1$, weak topological insulator (WTI) phase with weak index (001) in $-1 > m_0 > -2$, and WTI phase with weak index (111) in $-2 > m_0 > -3$.^{34,35)}

Let us first consider the features of surface states in the presence of small randomness. The situation is schematically described in Fig. 2. In the case of an STI or WTI(111), at $E \approx 0$, the surface states appear in x - y and y - z planes, but not in x - z plane, since we impose the periodic boundary condition in the y -direction. After integration over y , we expect amplitudes along the sides of x - z plane. On the other hand, the surface states at $E \approx 0$ appear only in the y - z planes for WTI(001), and the large amplitudes are expected along a z side. Whether they appear in the right z side or in the left depends on the configuration of random potential.

We set $W = 3.0$ and varied $m_0 \in [-1.8, -1]$ to teach the features of WTI(001), and $m_0 \in [-0.8, 0]$ to teach those of STI. These training parameters are along lines in W - m_0 plane, which are shown as dotted arrows in Fig. 3(a). To teach the features of DM, we set $W = 10.0$ and varied $m_0 \in [-2.5, 0.5]$, while for OI, we set $W = 3.0$ and varied $m_0 \in [0.2, 0.7]$. Actually, we do not know the phase diagram for the set of parameters we consider, so we assumed that changing $m_{0,z} = 1$ to 0.5 will not change the phase diagram drastically, and chose the parameters according to the knowledge of randomness-free case, $m_{0,z} = 0.5$ and $W = 0$, together with the information on the phase diagram for the isotropic but disordered case, $m_{0,z} = 1$ and $W > 0$.²⁷⁾

After teaching 4000 eigenfunctions in each phase, we prepared new 100×27 eigenfunctions with different m_0 (100 values) and W (27 values), and let the machine judge which phase each eigenfunction belongs to. We calculate the probabilities P_{OI} , P_{W001} , P_{SW111} , and $P_{\text{DM}} (= 1 - P_{\text{OI}} - P_{\text{W001}} - P_{\text{SW111}})$ that a given eigenfunction belongs to OI, WTI(001), STI or

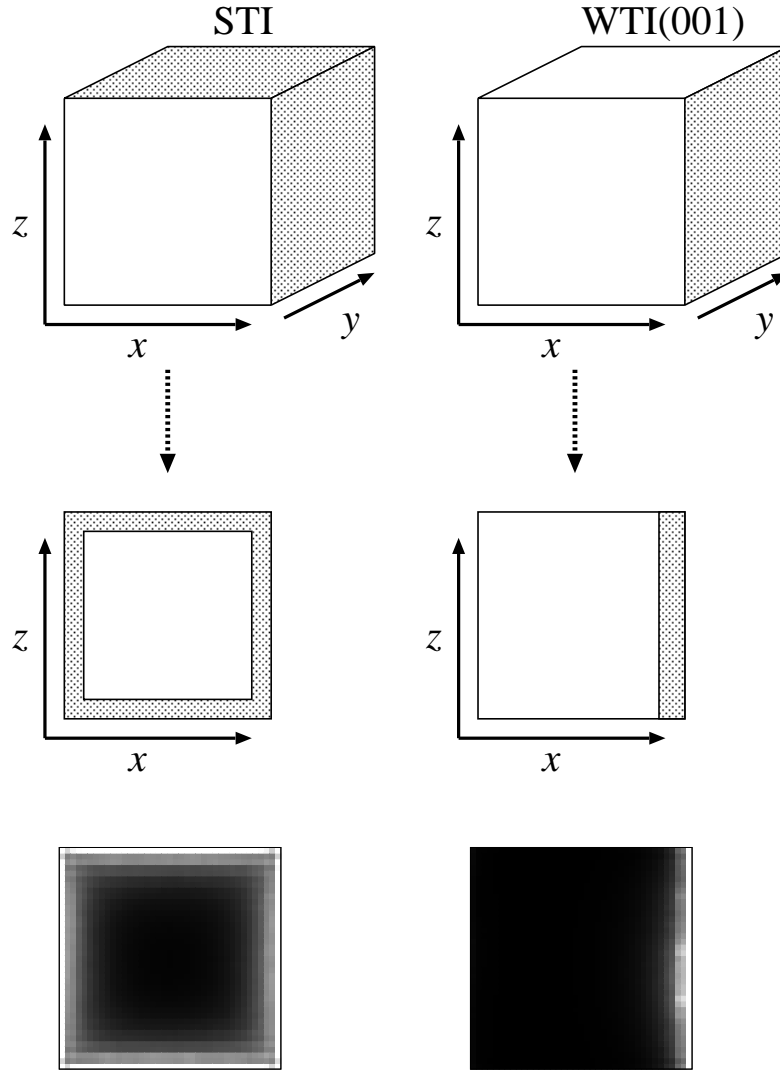


Fig. 2. Schematic of surface states in topological insulators, and the results of integration over y coordinate of numerically calculated eigenfunctions (bottom panels). Periodic boundary condition is imposed in y -direction, and fixed boundary condition in x - and z -directions. In the case of WTI(001), whether the strong amplitude region appears in the right ($x \approx 40$) or in the left ($x \approx 1$) depends on the specific configuration of randomness. In the bottom are shown numerically obtained modulus squared of eigenfunctions, where $(m_0, W) = (-0.16, 3)$ (STI, bottom left) and $(-1.16, 3)$ [WTI(001), bottom right].

WTI(111), and DM, respectively. Note that the present method cannot distinguish WTI(111) from STI, since WTI(111) contains surface states on all surfaces normal to x and z axes just as in STI, but from the behavior of randomness-free case, we can reasonably determine whether the phase is STI or WTI(111).

The probabilities of OI, WTI(001), STI or WTI(111), and DM are displayed as a color

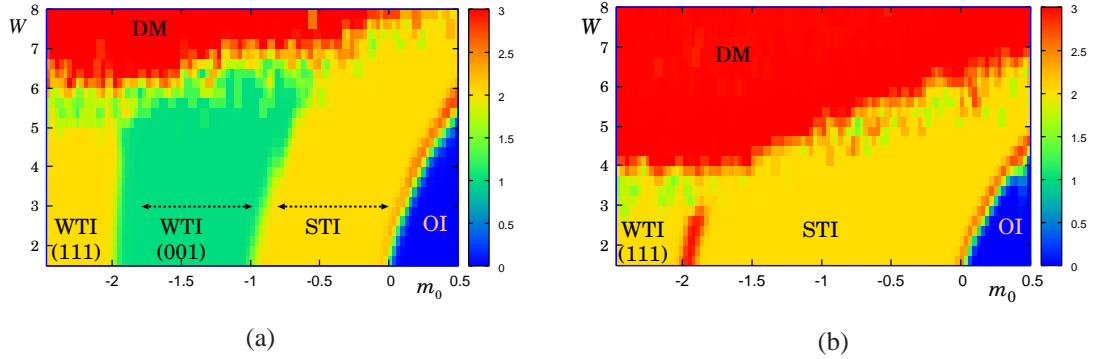


Fig. 3. Color map of P_{OI} , $P_{\text{W}001}$, $P_{\text{SW}111}$, and P_{DM} . The intensity $0 \times P_{\text{OI}} + 1 \times P_{\text{W}001} + 2 \times P_{\text{SW}111} + 3 \times P_{\text{DM}}$ is plotted. Shifts of the phase boundaries, OI/STI, STI/WTI(001), WTI(001)/WTI(111) by randomness is clearly seen. The arrows in (a) indicate the lines along which machine learning for STI and WTI(001) has been performed. The phase diagram where the transfer matrix method is not applicable, i.e., $t = m_{2z} = 1$ is displayed in (b).

map in the W - m_0 plane [Fig. 3 (a)]. We see that the phase boundaries between insulators with different topologies shift as we increase W . For example, when we start with OI phase, say $(m_0, W) = (0.3, 1.5)$ and increase disorder W , we enter into STI phase at $W \approx 6$. This is called the topological Anderson insulator (TAI) transition.^{36–38)} The present method captures TAI and gives a phase diagram quantitatively consistent with that obtained via the transfer matrix method.^{27,39)} It should be emphasized that one-dimensional training along a few finite lines in parameter space enables us to draw the 2D phase diagram.

We next apply the trained CNN of the above case, $t = 2$ and $m_{2z} = 0.5$, to the case of $t = m_{2z} = m_{2x} = m_{2y} (= m_2)$. In the absence of randomness, this choice of parameters gives OI for $m_0 > 0$, STI for $0 > m_0 > -2$, and WTI(111) for $-2 > m_0 > -4$.³⁴⁾ The standard method of using the transfer matrix²⁷⁾ to determine the phase diagram in the presence of disorder breaks down for this choice of parameters, since the transfer matrix connecting a layer to the next layer is not invertible for $t^2 - m_2^2 = 0$.²⁶⁾ This choice of parameters, therefore, demonstrates the wider validity of the machine learning method. Results are shown in Fig. 3 (b).

We note that although the colors of STI and WTI(111) are the same, we can distinguish them by the emergence of the metal phase (in fact, it is Dirac semimetal phase⁴⁰⁾) sandwiched between insulators with different topology. Whether they are STI or WTI(111) can be determined from the randomness-free limit.

3.3 Layered Chern insulator

We next consider two-dimensional Chern insulators,^{16,25,41)} and stack them in the z -direction to form three-dimensional Chern insulator (CI) and Weyl semimetal (WSM).^{16,42)} We begin with a spinless two-orbital tight-binding model on a square lattice, which consists of s -orbital and $p \equiv p_x + ip_y$ orbital,⁴³⁾ and stack them in the z -direction to form cubic lattice,

$$\begin{aligned} H = & \sum_{\mathbf{x}} \left((\epsilon_s + v_s(\mathbf{x})) c_{\mathbf{x},s}^\dagger c_{\mathbf{x},s} + (\epsilon_p + v_p(\mathbf{x})) c_{\mathbf{x},p}^\dagger c_{\mathbf{x},p} \right) \\ & + \sum_{\mathbf{x}} \left(- \sum_{\mu=x,y} (t_s c_{\mathbf{x}+\mathbf{e}_\mu,s}^\dagger c_{\mathbf{x},s} - t_p c_{\mathbf{x}+\mathbf{e}_\mu,p}^\dagger c_{\mathbf{x},p}) \right. \\ & \quad \left. + t_{sp} (c_{\mathbf{x}+\mathbf{e}_x,p}^\dagger - c_{\mathbf{x}-\mathbf{e}_x,p}^\dagger) c_{\mathbf{x},s} - it_{sp} (c_{\mathbf{x}+\mathbf{e}_y,p}^\dagger - c_{\mathbf{x}-\mathbf{e}_y,p}^\dagger) c_{\mathbf{x},s} + \text{H.c.} \right) \\ & - \left(t'_s c_{\mathbf{x}+\mathbf{e}_z,s}^\dagger c_{\mathbf{x},s} + t'_p c_{\mathbf{x}+\mathbf{e}_z,p}^\dagger c_{\mathbf{x},p} + \text{H.c.} \right), \end{aligned}$$

where ϵ_s , $v_s(\mathbf{x})$, ϵ_p , and $v_p(\mathbf{x})$ denote atomic energy and disorder potential for the s - and p -orbitals, respectively. Both $v_s(\mathbf{x})$ and $v_p(\mathbf{x})$ are uniformly distributed within $[-W/2, W/2]$ with independent probability distribution. t_s , t_p , and t_{sp} are transfer integrals between neighboring s -orbitals, p -orbitals, and that between s - and p -orbitals, respectively. t'_s and t'_p are interlayer transfer integrals.

As in ref.¹⁶⁾ we set $\epsilon_s - \epsilon_p = -2(t_s + t_p)$, $t'_s = -t'_p > 0$, $t_s = t_p > 0$, and $t_{sp} = 4t_s/3$, and take $4t_s$ as the energy unit. This set of parameters realizes a CI with a large band gap in the 2D limit, $\beta \equiv \frac{t'_p - t'_s}{2(t_s + t_p)} = 0$. As long as $1/2 > |\beta| \geq 0$, the system is fully gapped, which belongs to CI phase. The system enters into 3D WSM phase for $|\beta| > 1/2$.¹⁶⁾

In the presence of randomness, there appear four phases: CI, WSM, DM and AI. AI phase appears in large W region. Here we focus on the first three phases by considering $W < 4.5$ and $0.3 < \beta < 0.6$. Note that there is a correspondence between CI and WTI, and WSM and STI.⁴²⁾

As in the previous subsection, let us first consider the features of states near $E = 0$ in the case of small randomness. The situation is schematically described in Fig. 4, where periodic boundary conditions are imposed in y - and z -directions, while fixed boundary condition is imposed in x -direction. In the case of a CI, at $E \approx 0$, edge states run along y -direction, and after integration over y , we expect amplitudes in a dot in x - z plane close to a side along z -direction. On the other hand, in WSM, the surface states corresponding to Fermi arc¹⁴⁾ appear on surfaces normal to x -direction. Hence, large amplitudes are expected along z sides after integration along y . Owing to the presence of bulk Weyl node (shown as dilute dots) near the same energy $E = 0$, the right and left surfaces states are coupled and the high amplitude

regions appear on both right and left sides.

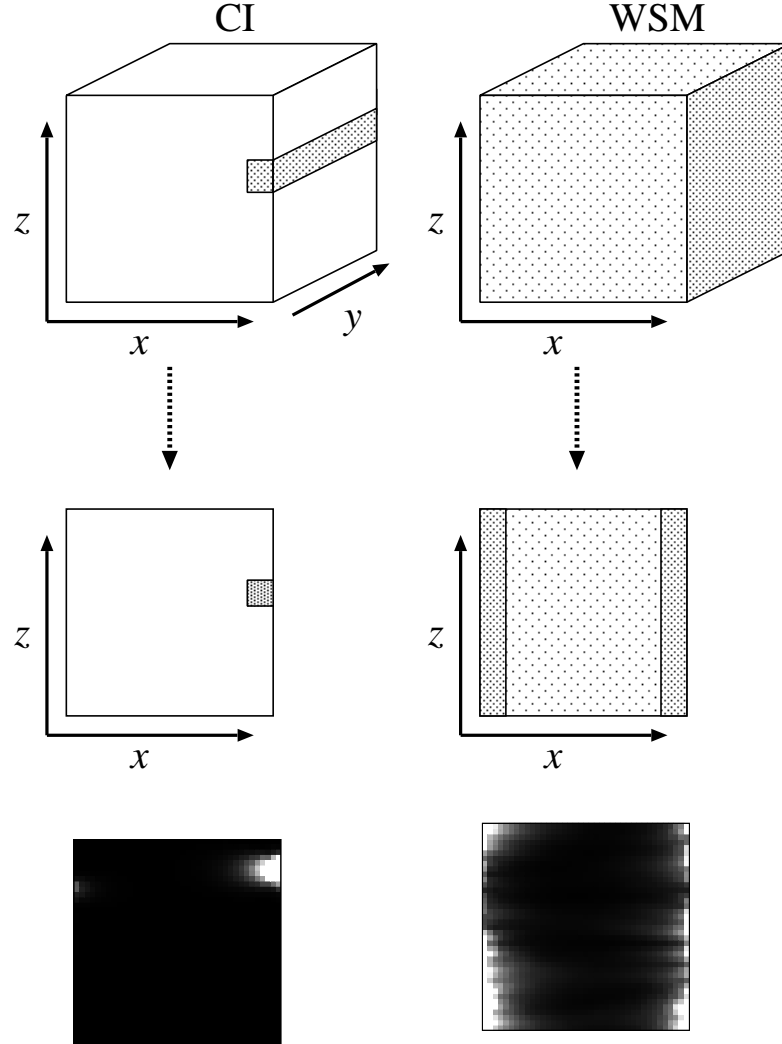


Fig. 4. Schematic of amplitudes and the results of integration over y coordinate of numerically calculated eigenfunctions (bottom). Periodic boundary condition is imposed in y - and z -directions, and fixed boundary condition in x . In the bottom are shown the modulus squared of numerically obtained eigenfunctions integrated over y . $(\beta, W)=(0.4, 0.6)$ (CI, bottom left) and $(\beta, W)=(0.55, 0.9)$ (WSM, bottom right).

We set $\beta = 0.4$ and varied $W \in [2.5, 4.5]$ to teach the features of DM, and $W \in [0.4, 1.6]$ to teach those of CI. For WSM, we set $\beta = 0.55$ and varied $W \in [0.3, 1.5]$. For DM and WSM, we have prepared 3000 samples for training the features of eigenfunctions, while 4000 samples have been prepared to teach the features of CI. We then varied β and W and let the machine calculate the probabilities P_{CI} , P_{WSM} , and $P_{\text{DM}} (= 1 - P_{\text{CI}} - P_{\text{WSM}})$ that a given eigenfunction belongs to CI, WSM, and DM, respectively. We then draw a color map in the

W - β plane as shown in Fig. 5, which well reproduces the phase diagram obtained by the transfer matrix method.¹⁶⁾

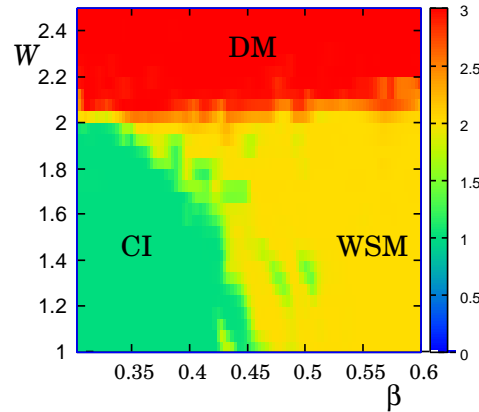


Fig. 5. Color map of P_{CI} , P_{WSM} , and P_{DM} . The intensity $1 \times P_{\text{CI}} + 2 \times P_{\text{WSM}} + 3 \times P_{\text{DM}}$ is plotted.

4. Summary and Concluding Remarks

In this paper, we have considered three examples of 3D quantum phase transitions: the Anderson transition, transitions in topological insulators, and transitions in Weyl semimetal. From the universality class point of view, the Anderson transition belongs to the orthogonal class, while topological insulators belong to the symplectic class. Weyl semimetal realized by stacking Chern insulator belongs to the unitary class. We therefore have covered all the three Wigner-Dyson classes.^{8–10)} Applications of this method to other 7 non-standard universality classes with chiral and/or particle-hole symmetries^{11, 12)} would be interesting.

By the machine learning, we could derive the approximate phase diagrams. In particular, the shift of phase boundaries between insulators with different topology as we increase disorder strength W has been captured. It should be emphasized that phase diagrams of topological insulators and Weyl semimetals have been determined by the results of learning along a finite one-dimensional lines in two-dimensional parameter space [see, for example, the arrows of Fig. 3 (a)].

The boundary between the DM and insulating phases such as OI, STI and WTI, on the other hand, are not as sharply determined as above. In the present calculations for topological insulators and Weyl semimetals, we did not take the ensemble average. Ensemble averages as well as finite size scaling would be necessary to determine the phase boundaries of diffusive metal phase more clearly, which is beyond the scope of the present paper.

In some systems, transfer matrix approach is not applicable. In this paper, we have demonstrated [Fig. 3(b)] that the deep learning method proposed here can be applied to systems where the transfer matrix is not defined. Other applications to complicated lattices such as quantum percolation^{44–47)} and fractal lattice⁴⁸⁾ are important future problems.

Machine learning has recently been applied to several problems of condensed matter physics such as Ising and spin ice models^{49,50)} and strongly correlated systems.^{51–56)} Applications to interacting electron systems with disorder such as Anderson-Hubbard model^{57,58)} as well as topological systems of dirty boson such as quantum magnon Hall insulator⁵⁹⁾ are interesting problems to be studied.

Acknowledgments

The authors would like to thank Koji Kobayashi for useful comments and for showing us a phase diagram corresponding to Fig. 3(a) obtained via the transfer matrix method prior to publication. Tomi Ohtsuki thanks Keith Slevin, Ken-Ichiro Imura, and Ryuichi Shindou for fruitful collaborations on 3D random electron systems treated in this paper. This work was partly supported by JSPS KAKENHI Grant No. JP15H03700.

References

- 1) P. W. Anderson: Phys. Rev. **109** (1958) 1492.
- 2) M. Z. Hasan and C. L. Kane: Reviews of Modern Physics **82** (2010) 3045.
- 3) X.-L. Qi and S.-C. Zhang: Rev. Mod. Phys. **83** (2011) 1057.
- 4) S. Murakami: New Journal of Physics **9** (2007) 356.
- 5) A. A. Burkov and L. Balents: Phys. Rev. Lett. **107** (2011) 127205.
- 6) A. P. Schnyder, S. Ryu, A. Furusaki, and A. W. W. Ludwig: Phys. Rev. B **78** (2008) 195125.
- 7) A. Kitaev: AIP Conference Proceedings **1134** (2009) 22.
- 8) E. P. Wigner: The Annals of Mathematics **53** (1951) 36.
- 9) F. J. Dyson: Journal of Mathematical Physics **3** (1962) 140.
- 10) F. J. Dyson: Journal of Mathematical Physics **3** (1962) 1199.
- 11) M. R. Zirnbauer: Journal of Mathematical Physics **37** (1996) 4986.
- 12) A. Altland and M. R. Zirnbauer: Phys. Rev. B **55** (1997) 1142.
- 13) L. Fu and C. L. Kane: Phys. Rev. B **76** (2007) 045302.
- 14) R. Okugawa and S. Murakami: Phys. Rev. B **89** (2014) 235315.
- 15) C.-Z. Chen, J. Song, H. Jiang, Q.-f. Sun, Z. Wang, and X. C. Xie: Phys. Rev. Lett. **115** (2015) 246603.
- 16) S. Liu, T. Ohtsuki, and R. Shindou: Phys. Rev. Lett. **116** (2016) 066401.
- 17) B. Sbierski and P. W. Brouwer: Physical Review B **89** (2014) 155311.
- 18) H. Katsura and T. Koma: J. Math. Phys. **57** (2016) 021903.
- 19) H. Katsura and T. Koma: arXiv:1611.01928 (2016).
- 20) T. Ohtsuki and T. Ohtsuki: Journal of the Physical Society of Japan **85** (2016) 123706.
- 21) T. Obuchi, H. Koma, and M. Yasuda: Journal of the Physical Society of Japan **85** (2016) 114803.
- 22) Y. LeCun, Y. Bengio, and G. Hinton: Nature **521** (2015) 436.
- 23) D. Silver *et al.*: Nature **529** (2016) 484.
- 24) Y. Asada, K. Slevin, and T. Ohtsuki: Phys. Rev. Lett. **89** (2002) 256601.
- 25) J. P. Dahlhaus, J. M. Edge, J. Tworzydło, and C. W. J. Beenakker: Phys. Rev. B **84** (2011) 115133.

- 26) S. Ryu and K. Nomura: *Phys. Rev. B* **85** (2012) 155138.
- 27) K. Kobayashi, T. Ohtsuki, and K.-I. Imura: *Physical Review Letters* **110** (2013) 236803.
- 28) Y. LeCun, L. Bottou, Y. Bengio, and P. Haffner: *Proceedings of the IEEE* **86** (1998) 2278.
- 29) Y. Jia, E. Shelhamer, J. Donahue, S. Karayev, J. Long, R. Girshick, S. Guadarrama, and T. Darrell: *arXiv:1408.5093* (2014).
- 30) X. Glorot and Y. Bengio: *Aistats* **9** (2010) 249.
- 31) T. Tieleman and G. Hinton: COURSERA: Neural Networks for Machine Learning **4** (2012) Lecture 6.5.
- 32) K. Slevin and T. Ohtsuki: *New Journal of Physics* **16** (2014) 015012.
- 33) C.-X. Liu, X.-L. Qi, H. Zhang, X. Dai, Z. Fang, and S.-C. Zhang: *Phys. Rev. B* **82** (2010) 045122.
- 34) K.-I. Imura, M. Okamoto, Y. Yoshimura, Y. Takane, and T. Ohtsuki: *Phys. Rev. B* **86** (2012) 245436.
- 35) K. Kobayashi, Y. Yoshimura, K.-I. Imura, and T. Ohtsuki: *Phys. Rev. B* **92** (2015) 235407.
- 36) J. Li, R.-L. Chu, J. K. Jain, and S.-Q. Shen: *Phys. Rev. Lett.* **102** (2009) 136806.
- 37) C. W. Groth, M. Wimmer, A. R. Akhmerov, J. Tworzydło, and C. W. J. Beenakker: *Phys. Rev. Lett.* **103** (2009) 196805.
- 38) H.-M. Guo, G. Rosenberg, G. Refael, and M. Franz: *Phys. Rev. Lett.* **105** (2010) 216601.
- 39) Koji Kobayashi, private communications.
- 40) K. Kobayashi, T. Ohtsuki, K.-I. Imura, and I. F. Herbut: *Phys. Rev. Lett.* **112** (2014) 016402.
- 41) C.-Z. Chang, W. Zhao, J. Li, J. K. Jain, C. Liu, J. S. Moodera, and M. H. W. Chan: *Phys. Rev. Lett.* **117** (2016) 126802.
- 42) Y. Yoshimura, W. Onishi, K. Kobayashi, T. Ohtsuki, and K.-I. Imura: *Phys. Rev. B* **94** (2016) 235414.
- 43) X.-L. Qi, T. L. Hughes, and S.-C. Zhang: *Physical Review B* **78** (2008) 195424.
- 44) Y. Avishai and J. M. Luck: *Phys. Rev. B* **45** (1992) 1074.
- 45) R. Berkovits and Y. Avishai: *Phys. Rev. B* **53** (1996) R16125.

- 46) A. Kaneko and T. Ohtsuki: *Journal of the Physical Society of Japan* **68** (1999) 1488.
- 47) L. Ujfalusi and I. Varga: *Phys. Rev. B* **90** (2014) 174203.
- 48) Y. Asada, K. Slevin, and T. Ohtsuki: *Phys. Rev. B* **73** (2006) 041102.
- 49) J. Carrasquilla and R. G. Melko: arXiv:1605.01735 (2016).
- 50) A. Tanaka and A. Tomiya: arXiv:1609.09087 (2016).
- 51) G. Carleo and M. Troyer: arXiv:1606.02318 (2016).
- 52) P. Broecker, J. Carrasquilla, R. G. Melko, and S. Trebst: arXiv:1608.07848 (2016).
- 53) K. Ch'ng, J. Carrasquilla, R. G. Mello, and E. Khatami: arXiv:1609.02552 (2016).
- 54) L. Li, T. E. Baker, S. R. White, and K. Burke: arXiv:1609.03705 (2016).
- 55) E. P. van Nieuwenburg, Y.-H. Liu, and S. D. Huber: arXiv:1610.02048 (2016).
- 56) L. Huang and L. Wang: arXiv:1610.02746 (2016).
- 57) H. Shinaoka and M. Imada: *Journal of the Physical Society of Japan* **78** (2009) 094708.
- 58) Y. Harashima and K. Slevin: *Phys. Rev. B* **89** (2014) 205108.
- 59) B. Xu, T. Ohtsuki, and R. Shindou: *Phys. Rev. B* **94** (2016) 220403.